REVERSE- AND CROSS-FLOW AERODYNAMICS FOR HIGH-ADVANCE-RATIO FLIGHT

Marilyn J. Smith
Associate Professor

Benjamin C. G. Koukol
Graduate Research Assistant

Daniel Guggenheim School of Aerospace Engineering
Georgia Institute of Technology, Atlanta, GA 30332-0150, USA

Todd Quackenbush
Senior Associate

Dan Wachspress
Senior Associate

Continuum Dynamics, Inc., Ewing, New Jersey 08618-2302 USA

Abstract

High-advance-ratio, high-speed rotorcraft flight enters complex aerodynamic regimes that, in many cases, have either been neglected or lie on the edge of models applied in comprehensive rotor code analysis. Specifically, rotor blades will experience large areas over the rotor disk where reverse-flow and cross-flow effects cannot be neglected during the design and analysis of an efficient rotor at high advance ratios. As experimental evaluations are expensive, a cost-effective alternative is the use of computational fluid dynamics (CFD) codes to develop sectional airfoil tables, as well as to understand the physics of these two flow effects. Numerical experiments have been performed, with correlation to experimental databases, that illustrate that CFD methods are an excellent alternative if advanced turbulence models are employed to correctly model the physics of separated and yawed flows. Correlation with an existing yaw equivalence model shows that corrections in the supercritical Mach range and high angles of attack tend to over predict the coefficients. At high radial flow conditions, the drag on the NACA0012 airfoil is equivalent to flat plate friction drag.

1. NOMENCLATURE

a	speed of sound, $\frac{ft}{sec}$
c	rotor blade chord length, ft
c_d	sectional drag coefficient
c_ℓ	sectional lift coefficient
c_m	sectional pitching moment coefficient
L'	sectional lift, $\frac{lbs}{ft}$
M	Mach number
r	rotor radial location, ft
R	rotor tip radius, ft
Re	Reynolds number
x, y, z	Cartesian streamwise,radial and normal lengths, ft
V	velocity, $\frac{ft}{sec}$
y^+	dimensionless wall spacing
α	angle of attack, deg
β	Prandtl-Glauert compressibility factor, $\sqrt{1-M^2}$
Λ	yaw angle, deg
μ	advance ratio, $\frac{U}{\Omega R}$
ω	dissipation per unit turbulent kinetic energy

Subscripts

$()_{ac}$	quantity at aerodynamic center
$()_{le}$	quantity at leading edge
$()_o$	incompressible quantity
$()_{2d}$	sectional quantity
$()_n$	normal quantity
$()_R$	radial quantity
$()_\infty$	free stream condition

2. INTRODUCTION

Significant analysis and design efforts on conventional rotors during the 1960s (e.g., Refs. 1–5) initially limited the upper limit of forward flight speed to an advance ratio of 0.5 ($\mu = 0.5$) based on the impact of retreating blade stall on the lift and propulsive force. This limit on performance diverted interest in high-speed rotorcraft designs towards the development of alternate configurations, such as the compound helicopter. As theoretical understanding, testing capabilities and computational methodologies advanced, the concept that high-speed forward flight may be achieved with conventional rotors

was revisited in the 1970s,[6–8] with the result that the theoretical forward flight limit speed was increased from 180 knots to 200-300 knots,[6] which was an improvement but did not attain the desired speed goals. During the 1980s and 1990s, most interest in high-speed rotorcraft development focused on alternate concepts,[9–11] primarily tiltrotor and tiltwing designs.

Recently, the rapid advance of technology in both hardware and software attained during the last two decades has sparked a number of new activities that have the potential to advance the capabilities of traditional rotor systems. New concepts, such as the Optimum Speed Rotor[12] and CarterCopter,[13] have identified potential payoffs of this overall approach in terms of improved efficiency at a range of flight speeds, including advance ratios greater than 1.0. The potential of achieving these high flight speeds without the penalties involved with tiltrotor technology is attractive, but as Johnson noted in 2005,[14] existing analysis tools and databases of aerodynamic information are inadequate to support the design of novel designs that could take advantage of these advanced concepts.

Thus in view of these advancements in technology and understanding of rotorcraft physics, the potential to achieve high-speed forward flight is being revisited through the analysis and design of conventional single or tandem/coaxial rotor concepts (e.g., Refs. 14–16).

3. MOTIVATION AND BACKGROUND

Sissingh[17] characterized the important flow regions over the rotor disk into three main aerodynamic regions: advancing, cross and reverse flows. These regions were delineated by simple angles for the purpose of investigating the stability of high-advance-ratio rotors. In order to study aerodynamic phenomena, this definition is expanded to show the interaction of the cross-flow and reverse-flow regions for various advance ratios, shown in Fig. 1. For the conventional rotor upper limit advance ratio of $\mu = 0.5$, the area of reverse flow (highlighted in a red dashed isocontour) is relatively small and the flow is primarily normal to the trailing edge. This is not the case when the advance ratio increases to the area of interest, namely between $\mu = 1.0 - 2.0$. The reverse-flow region increases over the retreating side of the rotor, while the magnitude and extent of the cross flow likewise increases. Thus, cross flow is important over a much larger range of Mach numbers and angles of attack, particularly within the reverse-flow region.

Figure 1 characterizes the need to understand the behavior of the rotor blade in these now significantly large regions of non-traditional flow if the aerodynamics of the rotor are to be resolved so that aeroelastic stability and performance analyses are to be accurately computed. These two regions have been studied independently of one another, so that most cross-flow research was investigated in forward-flight conditions ($V_n > 0$), and the body of research in reverse flow has been made for configurations in zero-yaw conditions ($\Lambda = 0$).

3.1. Reverse Flow

The influence of reverse flow on airfoil behavior was noted early in the development of rotorcraft and has been studied experimentally and numerically since the 1930's. There are two such works that provide comparisons at low Mach numbers across the entire range of angles of attack. Pope[18] at Georgia Tech quantified the flow over a two-dimensional NACA0015 airfoil in 1947 for a $Re = 1.2$ million at incompressible Mach numbers. Critzos *et. al*[19] followed in 1955 at Langley Research Center by studying a NACA0012 airfoil at $Re = 0.5$ million and $Re = 1.8$ million for an incompressible Mach number.

With the advent of computational methods, various studies have been undertaken to correlate with wind tunnel data and also to provide a method to generate airfoil characteristics in the absence of experimental facilities. The analyses by McCroskey[20] during the 1980's on the NACA0012 airfoil stand out among others as useful references when studying airfoil characteristics. In McCroskey's footsteps, the analysis by Bousman[21] of the SC1095 and SC1094 airfoil data and the subsequent computational correlations by Smith *et. al*[22] are also constructive. These later works do not include the full angle-of-attack analysis, so that reverse-flow characteristics are not included. They do however include transonic effects at lower angles of attack ($0^\circ - 30^\circ$) with which computational methods may be correlated.

3.2. Cross (Yawed) Flow

There have been several experimental studies of radial flow on non-rotating blades, principally the Purser and Spearman efforts[23,24] immediately following World War II, and the more recent studies by St. Hilaire *et. al*[25,26] and Lorber.[27,28] The former two studies were for a NACA0012 airfoil, while the latter study was for the Sikorsky SSC-A09 ($9\%c$ thickness, cambered) airfoil. Reported results show good correlation with the yaw equivalence equation[29] to force and moment coefficients for low Mach number and angle of attack. Combinations of run conditions that result in nonlinear interactions, such as stall and/or transonic flow, were noted to deviate substantially in some cases from the linear theory. The Purser and Spearman tests[23,24] were accomplished with finite wings of aspect ratio (AR) 3 and 6, resulting in induced velocity on inboard stations, as well as three-dimensional tip effects, so that the results were extrapolated to an infinite wing ($AR = \infty$). St. Hilaire *et. al*[26] noted that "...a major failure above stall for the cosine law normalization which has been shown to be consistently valid below stall."

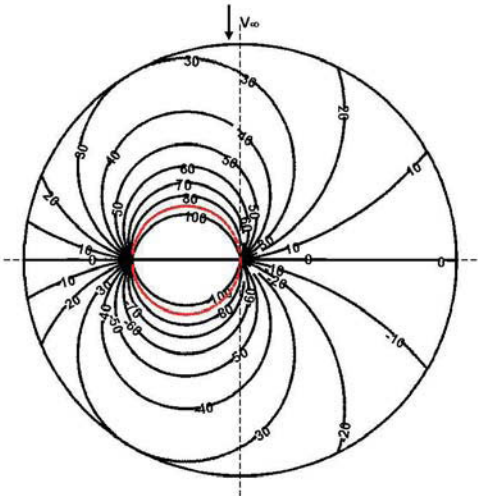

(a) $\mu = 0.5$

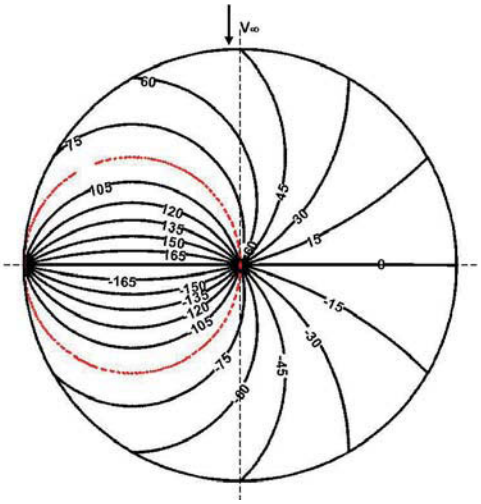

(b) $\mu = 1.0$

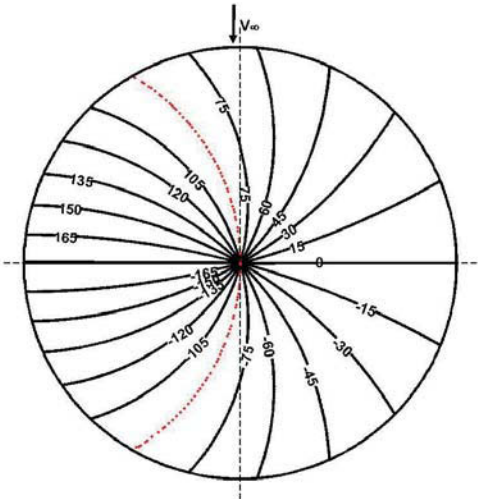

(c) $\mu = 2.0$

Figure 1: Characterization of the cross-flow and reverse-flow regions of a rotor in forward flight at differing advance ratios.

Harris recently performed a study of the ability of several comprehensive rotorcraft methodologies to predict rotor power at an advance ratio of 2,[30] but had no test data with which to correlate the results. All the analyses that he studied employed lifting-line blade aerodynamics models, as well as a CFD analysis, which suggests the presence of important and unanticipated radial flow effects that strongly affect the aerodynamic solution beyond the capability of existing modeling assumptions within the comprehensive codes. Quackenbush *et. al*[16] have subsequently modified the ability of their wake model to maneuver in these flight conditions, but the ability of current yaw equivalence corrections[29] over the expanded range of cross-reverse flow conditions that may be encountered in high-advance-ratio flight has not been verified to the knowledge of the authors.

3.3. Motivation

The motivation of this work is to explore and expand the understanding of the aerodynamic phenomena that rotor blades may encounter in high-speed, high-advance-ratio flight. This task also seeks to probe the potential of using computational experiments to generate data that capture the physics of the airfoil/rotor blade behavior accurately enough so that it can be applied in situations where wind-tunnel testing may not be feasible. These numerical experiments were correlated, in part, with existing experimental data and/or theory for validation. The numerical experiments conducted during this project were structured to address the fundamental need for additional data on high-advance-ratio rotor systems to both reveal key aspects of rotor behavior in this challenging regime and to provide additional data to correlate existing or develop new empirical models and expand the validation database.

Major advances in computer hardware over the past two decades have resulted in significant strides in the ability to resolve the Reynolds-Averaged Navier-Stokes (RANS) equations for rotorcraft via computational fluid dynamics (CFD) methodologies.[31] Further advances in the past decade have extended existing RANS turbulence models[32] that may have trouble resolving unsteady viscous-dominated flow field features, such as stall, separation, and shock-stall interactions. Researchers have made strides in adapting the turbulence simulation techniques used in large eddy simulations (LES) into a new class of hybrid RANS-LES turbulence simulation techniques that can be implemented into legacy RANS codes[33] to improve the ability of these CFD codes to predict integrated force and moment behavior of airfoils and wings at moderate cost.

4. COMPUTATIONAL MODEL

The numerical investigation for this work employed OVERFLOW,[34–36] a Reynolds-averaged Navier-Stokes

(RANS) methodology that resolves node-centered, structured meshes on either single block or Chimera[37] overset grid systems. A first-order implicit time algorithm achieves second-order integration via dual time stepping or Newton subiterations. Spatial discretization options include second- and fourth-order central differencing with Jameson's second-/fourth-order dissipation and Roe upwinding.[38] Low-Mach-number preconditioning is available for accuracy in computing low-speed steady-state flows. Boundary conditions are applied explicitly for all types of grids (O-,H-,C-), and periodic-boundary conditions for semi-infinite applications are available. Two versions of OVERFLOW, 2.0y and 2.1z, were used for the computations presented here.

4.0.1. Turbulence Modeling

For this study, several different turbulence models were applied to efficiently and accurately predict the flow field physics and airfoil behavior for differing flight conditions. These models include the Spalart-Allmaras one-equation turbulence model,[39] the Menter kω-SST two-equation turbulence model,[40] and two large eddy simulation (LES)-based models known as GT-KES[33,41,42] and HRLES-SGS.[43,44] The Spalart-Allmaras one-equation and Menter kω-SST two-equation turbulence models statistically model all of the length scales of turbulence and are collectively known with similar models as RANS turbulence models. RANS turbulence models have been classically associated with computational fluid dynamics (CFD) RANS codes, as they are numerically efficient for grids that are suitable for production computations in engineering environments. Because these models are statistical models of the turbulence behavior over both time and length scales, they include coefficients that are *tuned* using a set of test cases that range the spectrum of aerospace applications, rather than a specific application. The coefficients are typically chosen as the values that provide fairly comparable levels of accuracy across the set of test cases. In many applications, these models may also neglect the terms in the spanwise (radial) direction, permitting larger computational cell aspect ratios in the span direction while reducing computational requirements, but at the cost of capturing all of the features of three-dimensional flows.

The other two methods are part of a relatively newer class[32,45] of turbulence simulation techniques known as hybrid LES-based methods. These techniques are derived from more costly LES where the larger scales of turbulence are numerically captured, leaving only the smaller turbulent scales to be statistically modeled. These models have been implemented into legacy RANS codes for use in less costly simulations. These LES-based techniques by definition should provide more physically correct representations of unsteady and/or separated flow fields, even on production RANS grids that are considerably coarser than traditional LES grids. This has been demonstrated[33,43,46] for a number of configurations of interest to rotorcraft.

4.0.2. Run Conditions

Simulations were computed using the OVERFLOW (versions 2.0y and 2.1z) code with the 4^{th}-order central-difference scheme along with the ARC3D diagonalized Beam-Warming scalar pentadiagonal scheme. Dissipation was calculated using the TLNS3D dissipation scheme. The 4^{th}-order smoothing coefficient was set to the default of 0.04, and the 2^{nd}-order smoothing coefficient was set to 0.0 for subsonic and 2.0 for transonic flows. Different turbulence simulation closure methods were applied depending on the level of unsteadiness found in the flow physics.

RANS turbulence models have been shown[22,47] to have difficulty predicting the character of stall for some airfoils, while LES-based models have been able to capture the performance characteristics more accurately.[47] Therefore, for angles of attack above stall at each Mach number, the turbulence model was changed from the Menter kω-SST RANS to the kinetic eddy simulation (KES) and HRLES-SGS models, described earlier. These runs require that time-accurate simulations be computed. To ensure that the two models are compatible, at low angles of attack the predictions were compared and found to be within 5% of one another. Since these turbulence closures are LES-based, they should be run in full three-dimensions as a infinite wing, which significantly raises the cost of the simulations. In addition unsteady post-stall angles of attack require time-accurate solutions. The HRLES-SGS model is less expensive (2-3%) than KES and was applied for most of the CPU-intensive simulations. It also has the advantage of devolving to its RANS Menter kω-SST model at low angles of attack for consistency across the angle of attack regime.

Unsteadiness in the force or moment simulations, indicating shed vorticity and/or separation is depicted using error bars about each computational data point. In these circumstances, the mean data point was computed by averaging the data over a minimum of three periodic cycles. The error bar limits indicate the average of the minimum and maximum values of the data cycles used to compute the mean.

5. CORRELATION DATA

The configuration for these studies was chosen to be the NACA0012 airfoil. The airfoil numerical simulations were correlated with results from existing experimental campaigns, most notably the incompressible tests reported by Abbott and Von Doenhoff[48] and Critzos *et. al*,[19] as well as the more recent wind tunnel correlation study of McCroskey,[20] which includes compressible data.

The two-dimensional NACA0012 campaign of Critzos *et. al*[19] analyzed angles of attack from $0^\circ - 180^\circ$ at $Re = 0.5 \times 10^6$ and $Re = 1.8 \times 10^6$ in the NASA Langley low-turbulence wing tunnel. Maximum Mach number was limited to 0.15. Roughness effects were also examined as part of the campaign. Reynolds number and roughness effects were noted to have only a small impact on the integrated forces and moments except for angles of attack near 180°. The model was reported to have a maximum deviation of no more than 0.003 inches from the analytical model. Blockage corrections were added to the data based on theoretical derivations. The forces and moment were measured using a multicomponent strain gage balance. Uncertainties in the lift, drag and pitching moment (quarter-chord) coefficients were determined to be ± 0.049, ± 0.016 and ± 0.017, respectively, for $Re = 0.5 \times 10^6$ runs, and ± 0.017, ± 0.006 and ± 0.006, respectively, for $Re = 1.8 \times 10^6$ runs.

Pope conducted a campaign[18] at Georgia Tech for an eighteen inch chord in the $2.5' \times 9'$ two-dimensional wind tunnel for an angle-of-attack sweep from $0^\circ - 180^\circ$. The Reynolds number per chord was 1.23×10^6 for the nominal speed of 80 mph ($\approx 0.1M$). The smooth test model was ascertained to have a maximum deviation of no more than 0.005 in. from the analytical model. Forces and pitching moment (about quarter chord) coefficients were obtained from a balance and by integration from pressure taps at every 0.05 x/c from 0. to 1., augmented by taps at x/c =0.0125, 0.025, 0.075, and 0.975. Pressure coefficient data at selected angles of attack are also available. Tunnel corrections were computed and found to be 0.06° and were neglected in the final coefficient data. No numerical estimates of the uncertainties in the data were provided. Critzos noted that these (Pope's) data were low for a NACA0015 but they do provide a basis for correlation if some care is taken, and if this caveat is noted.

The classic data from Abbott and Von Doenhoff[48] was also utilized as a third set of incompressible data at low angles of attack to aid in pitching moment evaluations. The pitching moments were measured by a balance, and no tunnel corrections were applied. The data were available at $Re = 3 \times 10^6$, 6×10^6 and 9×10^6. Experimental uncertainties were not specifically identified by numerical value.

6. COMPUTATIONAL GRIDS

Several different structured grids were used in this study. The sectional characteristics study was computed with two different grid topologies to study the impact of the trailing edge configuration, as well as two different streamwise grid distributions to capture low and high angle-of-attack flow features. Grid studies were performed for these grids at two different angles of attack, one within the linear region and the other in the post-stall region. The final grids used for this study were observed to provide integrated force and moment results comparable to finer grids when flow was attached, as well as averaged results within 2–4% of one another for separated flows.

An O-grid was generated to evaluate the influence of the finite trailing edge, as observed in Fig. 2(b). This grid consists of 120 points normal to the airfoil surface and 825 along the circumference of the airfoil. The 825 streamwise points were divided equally among the upper and lower surfaces of the airfoil. The initial cell spacing normal to the surface is $5.0 \times 10^{-6}c$, which represents a $y^+ \leq 1$ for the range of Reynolds numbers evaluated in the study. The outer boundary location was evaluated at $5c$, $15c$, and $30c$ distances from the airfoil. For very large angles of attack ($> 30^\circ$), the smaller outer boundaries were not capable of capturing the large amount of unsteady effects present in the airfoil wake, although for smaller angles of attack, the resulting integrated forces and moments were not influenced.

In many structured CFD analyses, the realistic trailing edge of the airfoil is not modeled in order to minimize the number of grid points and minimize grid skewness caused by modeling the sharp corners of the trailing edge. So that the impact of the trailing edge modeling could be evaluated, in particular during reverse-flow conditions, a C-grid (Fig. 2) was generated to mimic common practice in grid generation for airfoils with sharp trailing edges. The C-grid parallels the setup of the O-grid in terms of the normal mesh spacing. The C-grid contains a total of 1105 nodes, with 807 points equally divided between the upper and lower airfoil surface.

Typical airfoil grids also cluster nodes in the area within $1c$ normal to the airfoil surface, as the wake remains primarily in this area for small to moderate angles of attack. For large angles of attack this is not an optimal grid spacing, so that a second grid was generated with a more appropriate meshing to capture the wake flows. This modified grid increased the streamwise surface nodes to 971, locating 609 on the upper surface and 362 on the lower. The number of normal grid mesh points was also increased to 200 to permit a more dense grid distribution to extend further into the far field, which becomes the wake at angles of attack approaching 90°. Since this airfoil is symmetric, only positive angles of attack were needed to characterize the airfoil behavior. The modified grid is illustrated in Fig. 3. The remainder of the grid characteristics remained constant with the original grid. The impact of this grid modification can be readily observed in Fig. 4. The original O-grid from Fig. 2 coarsens in the wake where a leading edge vortex is being shed and tends to dissipate the strength of the shed vortex, as well as to translate the location of the vortex, modifying its interaction with the trailing edge wake. This causes

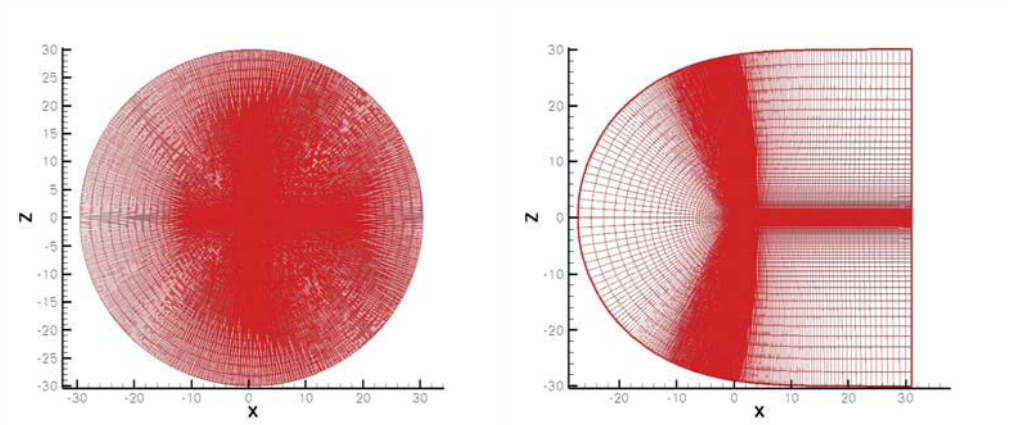

(a) Full grid

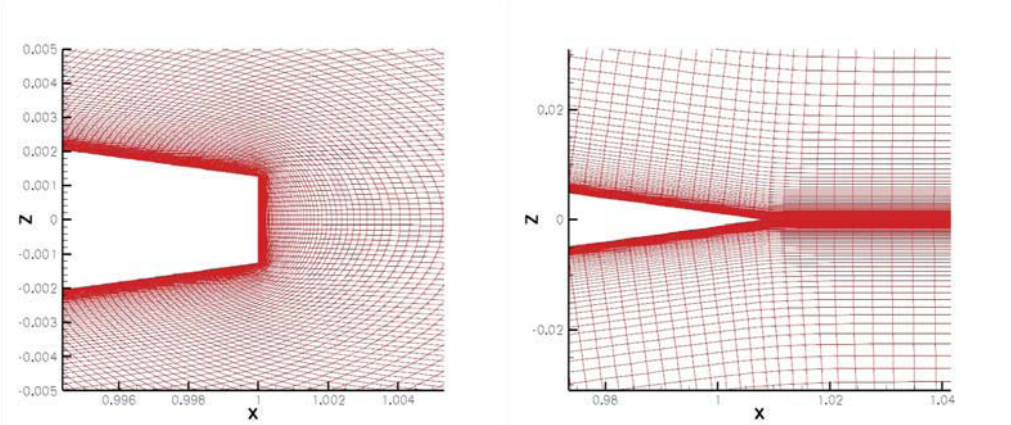

(b) Closeup of trailing edge

Figure 2: Two-dimensional grids. O-grid with blunt trailing edge is on the left, and an C-grid with sharp trailing edge is on the right.

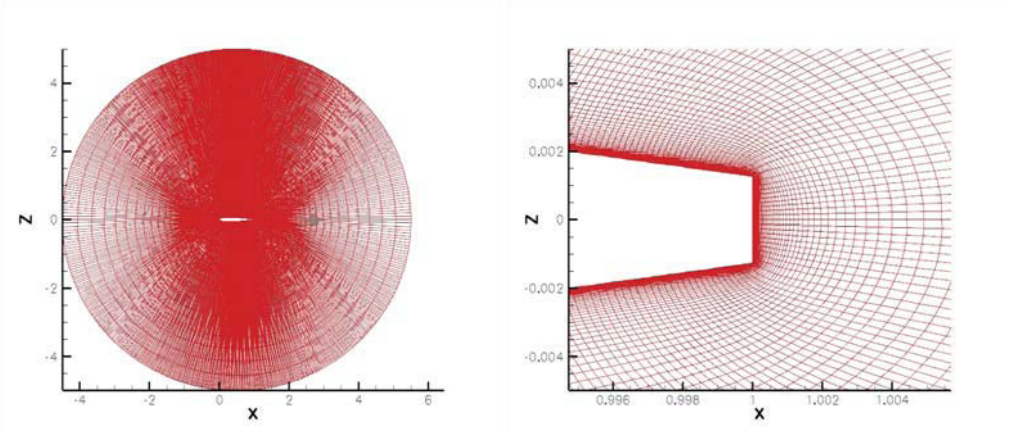

Figure 3: Modified two-dimensional O-grid for high angle-of-attack simulations.

abrupt shifts in the integrated forces and moments that are not observed in experiment.[18,19]

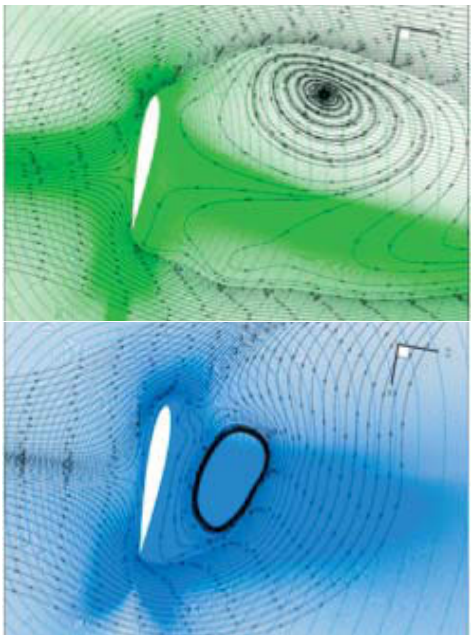

(a) Streamlines overlaid with vorticity contours (Upper: original grid, Lower: redistributed grid)

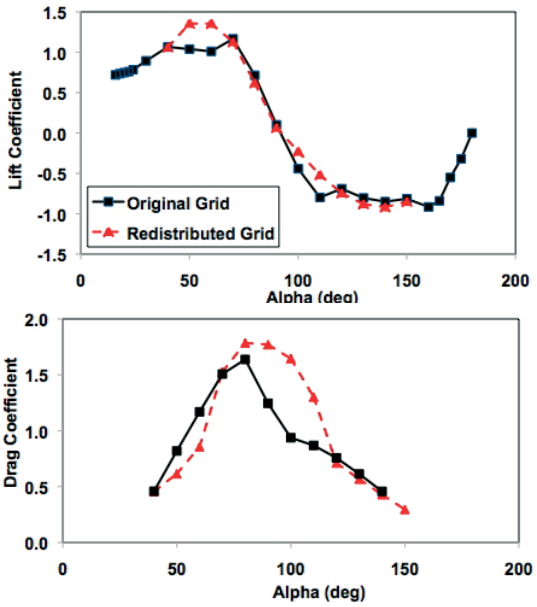

(b) Lift and drag coefficient

Figure 4: Influence of the grid on high angle-of-attack simulations.

To study cross flow and large separated flows, three-dimensional grids were created based on the higher fidelity (high angle of attack) two-dimensional grid. Each two-dimensional grid was stacked to form an O-H or C-H grid. The boundary condition at the end of the radial (spanwise) extent of the grids is a periodic boundary so that an infinite span wing could be modeled. Radial (spanwise) extents of $1.0c$, $2.0c$, $4.0c$ and $8.0c$ were studied, along with the number of radial planes to capture the three-dimensional flow for the infinite span wing. Many of the high angle-of-attack flight conditions could be accurately captured with a span of $2.0c - 4.0c$ and 61 spanwise planes, while the yawed flow required $4.0c - 8.0c$ and 121 spanwise planes to adequately resolve the periodic shedding at higher angles of attack.

7. RESULTS

7.1. Airfoil Characteristics

The first evaluation undertaken in the study was that of the airfoil characteristics that are applied to various comprehensive analyses in the form of look-up tables of integrated lift, drag and pitching moment over the range of Mach numbers and angles of attack that the blade section is expected to encounter. Look-up tables are developed by various methods, including numerical, experimental, theoretical results and/or combinations thereof. Airfoil characteristics are usually well-defined at lower angles of attack and lower Mach numbers. Unfortunately, the characteristics that can be the most critical are for stalled and transonic flows where the data are more sparse and the physics is complex and less understood. In addition, the behavior of the airfoil in reverse flow is increasingly critical as the advance ratio of the rotor rises above 1.0, immersing the rotor in larger regions of reverse flow, as illustrated by Fig. 1. Thus, the ability to identify the airfoil characteristics over the entire range of angles of attack and Mach spectrum was explored via numerical means, correlated by prior experimental results to determine best numerical practices for future simulations.

Force and moment data about the NACA0012 airfoil were generated for Mach numbers from $0.1 - 1.0$, in increments of 0.1. The angle-of-attack range included angles from $0° - 180°$, which permitted the entire $360°$ spectrum to be predicted, given the airfoil symmetry. For the primary flow direction, which the rotor is most likely to encounter, angles of attack from $0° - 24°$ in increments of $2°$ were simulated. Increments of $10°$ were utilized from $30° - 160°$ degrees, with smaller increments of $2°$ or $5°$ applied from $160° - 180°$ where the airfoil is once again experiencing attached flow.

The initial correlation was made at incompressible Mach numbers to correlate with Critzos[19] and Pope[18] over the entire range of possible angles of attack, as shown in Fig. 5. Pope also published pressure coefficient data

for the NACA0015 airfoil over the angle of attack range. While Critzos noted that this (Pope's) data set was low for a NACA0015, it is similar to the NACA0012 in some regions, and so it is used as a basis to evaluate the ability to capture the pressure distributions of the numerical simulations, as noted in Fig. 6.

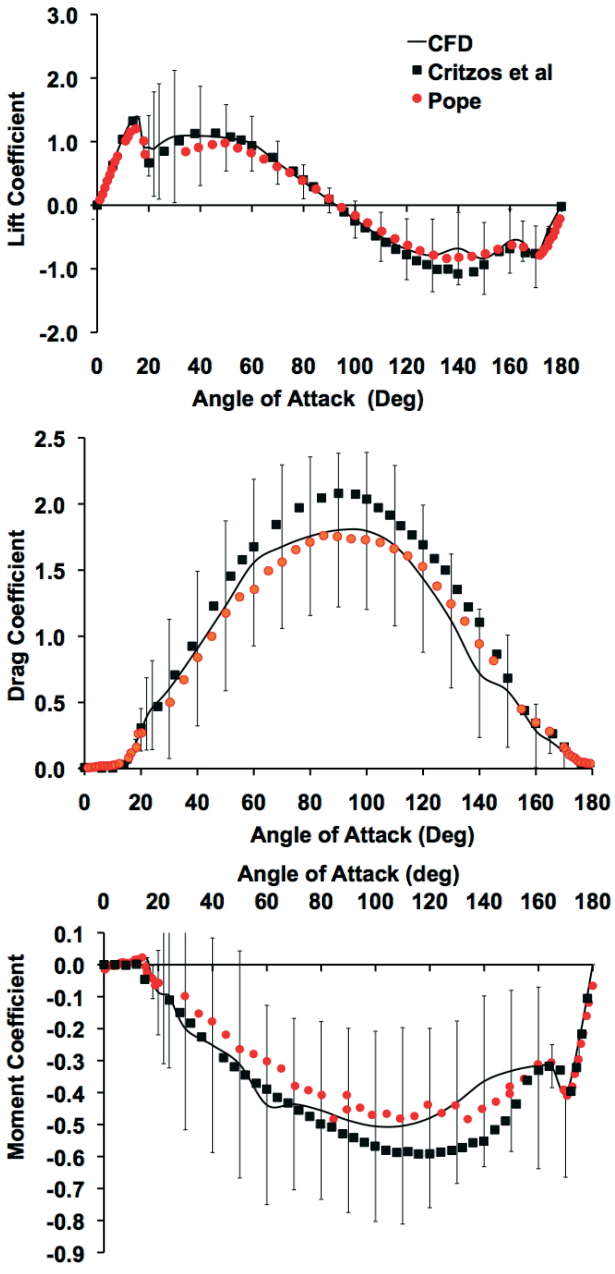

Figure 5: Mach 0.1(incompressible) sectional airfoil characteristics

7.1.1 Low to Moderate Angles of Attack

The computational methodology was first correlated against the incompressible and low subsonic Mach regimes at low to moderate angles of attack to correlate with experimental and theoretical data. Most of these flight conditions were able to be accurately resolved using steady-state simulations by RANS turbulence models below stall. Examples of the typical force and moment data this subset of data are presented in Fig. 7. For ease in analyzing the data, error bars denoting the experimental uncertainties were not included in the figure. It should also be noted that at these expanded scales, errors in digitization of the experimental data from plots may be magnified. Similar to the conclusions of Critzos, the CFD simulations at the two different Reynolds numbers do not show significant differences. Comparisons with the NACA0012 experiment show good correlation with all coefficients below stall. Various experiments[19,48,49] report the stall break from about a $c_\ell = 1.4$ at $\alpha = 16^\circ$ for Reynolds numbers about 1×10^6 to a high of $c_\ell = 1.6$ at $\alpha = 17^\circ$ for Reynolds numbers about 2×10^6 and higher. Critzos reports stall break at the lower of these values, with roughness effects reducing the magnitude of $c_{\ell_{max}}$ even further. The Critzos drag and pitching moment data were presented at plot scales that did not provide sufficient resolution for correlation, so that data from Abbott and von Doenhoff[48] and Jacobs and Eastman[49] were also compared with the computational results.

Profile drag values from Abbott and von Doenhoff at $Re = 3 \times 10^6$ and Jacobs and Sherman tabulate $c_{d0_{min}}$ values that are $10 - 20$ counts lower than the computational results. The computational results also are within $2 - 5$ counts of drag compared the experimental equation for $c_{do_{min}}$ reported by McCroskey.[20] The pitching moment slope in most reported experiments is essentially zero about the quarter-chord, as expected from thin airfoil theory. The computational results are zero until approximately $4^\circ - 5^\circ$ angle of attack, when viscous effects begin to take effect. The character of the drag rise with both Critzos and Abbott and von Doenhoff appears to be captured. The moment break occurs at the stall location, and is consistent with the reported correlation with wind tunnel results for lift coefficient. This is consistent with the pressure coefficient correlation for $\alpha = 10^\circ$ shown in Fig. 6(a), as in this range the integrated values are very close for both airfoils.

As the Mach number increases within the range of subcritical Mach numbers ($M_\infty < 0.5$), McCroskey[20] verified that the application of the Prandtl-Glauert compressibility correction, $\beta = \sqrt{1 - M^2}$, fell within the limit of the experimental values and described the experimental lift curve slope variation (within $\pm 2\%$) as

$$\beta C_{\ell_\alpha} = 0.1025 + 0.004851 log\left(\frac{Re}{10^6}\right) \quad (1)$$

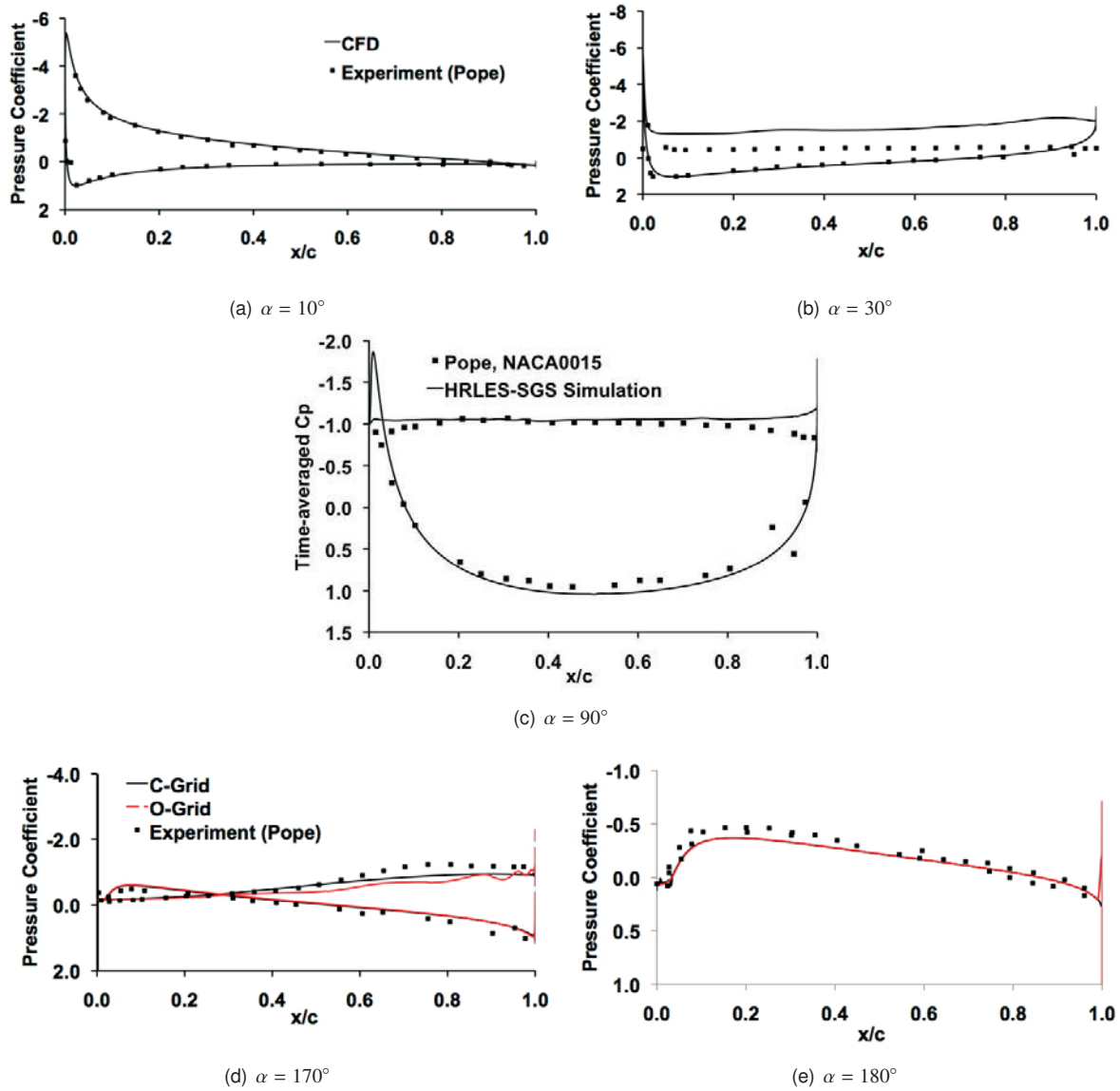

(a) $\alpha = 10°$

(b) $\alpha = 30°$

(c) $\alpha = 90°$

(d) $\alpha = 170°$

(e) $\alpha = 180°$

Figure 6: Mach 0.1(incompressible) pressure coefficients compared with Pope.[18] Subfigures (d) and (e) illustrate the role of the grid in reverse flow.

Within the linear regime, the CFD data predict lift curve slopes that primarily fall within the experimental error of Eqn. 1. The maximum lift coefficient values vary in their correlation with experimental data. For Mach numbers up to 0.8, the numerical predictions fall within the experimental error limits for approximately half of the cases, or 35% below the minimum error limit for the remainder of the cases.

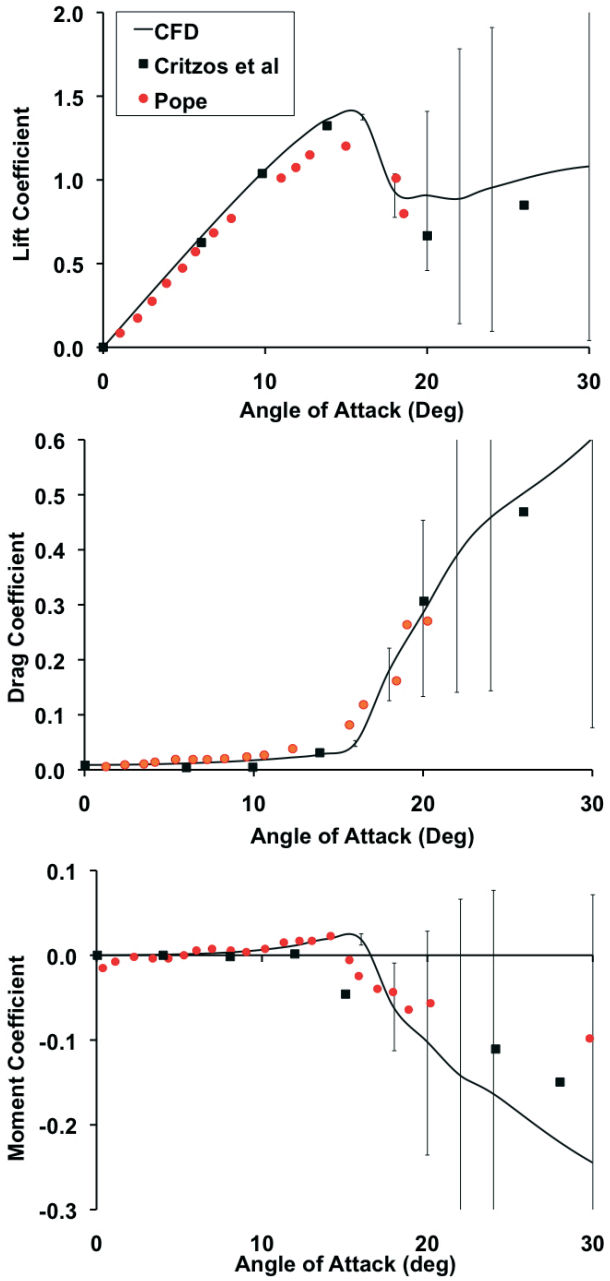

Figure 7: Mach 0.1 (incompressible) comparisons of kω-SST RANS simulations with Critzos[19] and Pope[18] experiments.

The minimum drag coefficient is also compared to the results of McCroskey's experimental analysis.[20] Much like the lift curve slope, the experimental minimum drag coefficient at Mach numbers below the drag divergence ($M_\infty < 0.75$) can be estimated by one equation (within ± 0.0005) based on the Reynolds number:

$$C_{d_o} = 0.0017 + \frac{0.91}{(log(Re))^{2.58}} \quad (2)$$

The value for minimum drag was thus observed to remain relatively constant with respect to Mach number for completely subsonic flow. The CFD predictions for minimum drag fall within the 0.0005 error range, which equates to 4.7% and 5.6% error for the 1 and 5 million Reynolds number, respectively. The data at 5 million Reynolds number are very close to the experimental mean compared to the data at 1 million Reynolds number, which has a maximum error of 7% at the upper limit of Mach 0.7.

Lift to drag ratios are significantly lower for the computational RANS estimates compared with the experimental data, which parallel the findings noted in Ref. 22, although the L/D findings are improved with the advanced LES turbulence methods near stall. Note that at low angles of attack, the HRLES-SGS model becomes the RANS model upon which it is based, so there should be no change in characteristics. Specifically the small under prediction of lift curve slope and maximum lift, combined with the slight over prediction in drag yield significantly smaller L/D ratios with respect to the experimental predictions. The L/D experimental error is approximately 10% about the mean, however, the computational L/D values under predict the mean by as much as 50%. This finding is consistent with Smith *et. al*'s evaluation[22] of the SC1095 airfoil using a number of different CFD simulations with RANS turbulence models.

Returning to the incompressible experimental data, the influence of modeling a realistic versus idealized trailing edge can be determined by comparing the results of the comparably sized C- and O-grids, as previously shown in Fig. 2. Not unexpectedly, as angles of attack are increased, there is earlier surface pressure unsteadiness from the O-grid resulting from the shed vorticity which forms at the finite trailing edge which acts as a bluff body, as illustrated in Fig. 8. For subsonic Mach numbers, the typical differences observed between the two grids for the lift coefficient is less than 1.5% until the stall region where the differences moderately increase to approximately 3%. At zero lift, the friction drag dominates, resulting in a 5% difference that drops to 1% or less as angle of attack is increased until stall where it rises abruptly to 5-10% error as viscous effects again dominate. There is a significant difference in the pitching moment (referenced to the quarter chord), which varies from 20% to 100%.

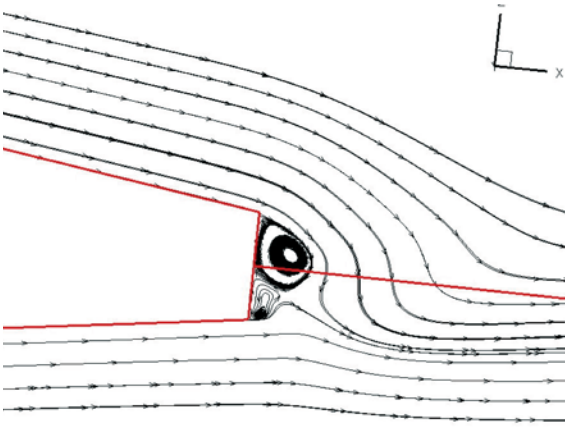

Figure 8: Example of the blunt trailing edge flow separation with the O-grid.

It should also be noted that with these numerical results, the standard thin airfoil theory assumption of the quarter chord location as the aerodynamic center should be approached with caution. The aerodynamic center is defined as the location where the pitching moment does not change with angle of attack, which for a symmetric airfoil should be a zero pitching moment for the angles of attack below stall ($\approx 11^\circ - 12^\circ$). This holds for inviscid theory, but will break down as viscous effects begin to influence the pitching moment. Both Critzos and Pope report non-zero slopes at the quarter chord location, indicating a shift in the aerodynamic center from the quarter-chord, most likely due to model irregularities and/or testing apparatus. While the O-grid results which deviate only slightly from a zero pitching moment could be partially attributed to the blunt trailing edge, the more significant deviation from the assumed values is for the simplified C-grid. However, this deviation can be easily explained via an analysis that computes the actual aerodynamic center based on the computational results. That is, moment coefficient at any location on the airfoil within the linear range can be computed using the formula

$$c_{m_{ref}} = c_{m_{le}} + c_\ell \left[\left(\frac{x}{c} \right)_{ref} - \left(\frac{x}{c} \right)_{le} \right] \tag{3}$$

If the reference point is chosen to be the aerodynamic center, then the moment will not change with angle of attack, leading to the relation

$$\frac{dc_{m_{ac}}}{d\alpha} = 0 = \frac{dc_{m_{le}}}{\alpha} + \frac{dc_\ell}{d\alpha} \left[\left(\frac{x}{c} \right)_{ref} - \left(\frac{x}{c} \right)_{le} \right] \tag{4}$$

Using the results of the CFD computations, the moment slope at the leading edge can be computed using

$$\frac{dc_{m_{le}}}{d\alpha} = 0 = \frac{dc_{m_{x/c=0.25}}}{\alpha} + \frac{dc_\ell}{d\alpha}[0.25] \tag{5}$$

Using this analysis on the computational C-grid data, the aerodynamic center is found to be between $x/c = 0.24 - 0.243$ for Mach numbers ranging from 0.1 to 0.5. Conversely, the O-grid data shows the aerodynamic center to be located between $x/c = 0.248 - 0.249$ for the same Mach range. An example of the corrected pitching moment at the aerodynamic center for the C-grid is shown in Fig. 9. The pitching moment is now essentially zero until an angle of attack of approximately 8° is reached. This behavior is now comparable to the behavior of experimental test data for the NACA 4-series airfoils.[18–20, 48]

This behavior can be explained by observing the computational grid near the trailing edge (Fig. 2). While for the O-grid, the blunt trailing edge at $x/c = 1.0$ is specifically modeled, the blunt trailing edge in the C-grid is closed by the first coincident grid point in the wake. This results in an extended chord on the computational grid, which will very slightly modify the force coefficient computation ($< 0.2\%$), as well at the computation of the moment coefficient. For this instance, the chord is extended to a value of 1.009, which moves the quarter-chord location to $0.2522c$, and results in the differences reported earlier.

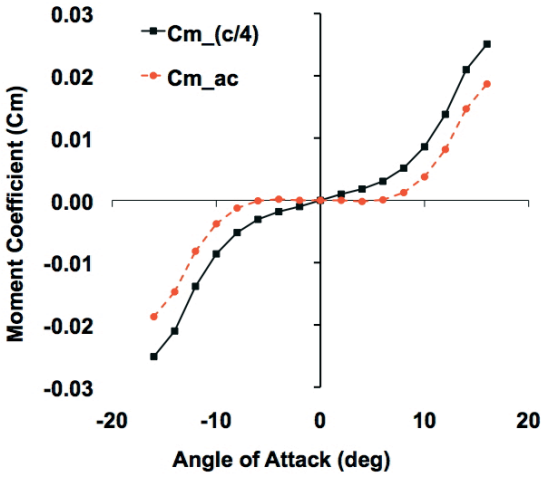

Figure 9: Example of the pitching moments obtained by the two-dimensional C-grid, corrected for the extended chord.

7.1.2 Large Angles of Attack ($20^\circ - 160^\circ$)

The CFD runs were continued beyond the traditional $20^\circ - 24^\circ$ angle-of-attack sweep to include all angles in separated flows up to 160° degrees. At these very large angles of attack, the leading edge behaves similar to a circular cylinder, albeit under the influence of the trailing edge, which acts as a discrete separation point. As the angle of attack approaches 90° from either direction, the airfoil will continue to lose lift, while the drag will approach that of a flat plate. The limiting drag coefficient of a infinite flat plate perpendicular to a flow is approx-

imately 2.0,[50] and at incompressible Mach numbers is observed experimentally[18,19] to approach $1.6 - 2.0$. Critzos notes that Wieselsberger[51] conducted experiments for flat plates at $90°$ angle of attack and found that as aspect ratio is reduced, the drag coefficient reduces from 2.0; the value cited was for an aspect ratio of 20 resulting in a drag coefficient of about 1.48. This implies that although the grid and periodic boundary condition combination in the numerical simulation was "converged", the boundary condition may still be imposing an aspect ratio effect. The drag was observed to be relatively insensitive to Reynolds number at these high angles of attack. Comparison of the averaged pressure coefficient with experimental data[18] shows very good correlation (Fig. 6(c)) for the midspan section. Note that as the behavior of the airfoil at this angle of attack should approach that of a flat plate, only minor differences due to the thickness should be observed, primarily at the curved leading edge.

As the angle of attack is increased to $\alpha = 30°$ differences between the simulation and the experimental data begin to appear. The time-averaged numerical pressure coefficients indicate that the upper surface separates approximately $2 - 3\%$ earlier than the experimental data, which will account for the differences in the moment coefficient. In addition, there may well be differences that are due to the periodic boundary condition noted above, or it could be due to the averaging technique of the time-accurate numerical simulation compared to the experiment. While care was taken to ensure that a periodic solution over several cycles was used to generate the characteristics, it is not known how the experimental values were time-averaged. Similar behavior is observed throughout this range, though it should be noted that the integrated forces and moments trends are very similar between the numerical and experimental data.

7.1.3 Reverse-Flow Angles of Attack ($160° - 180°$)

At high angles of attack near 180 degrees, the airfoil is operating in a reverse-flow region, where the free stream now flows first over the trailing edge. In this region, Critzos[19] provides a description of the flow observed in the experiment:

> WIth the airfoil producing positive lift near an angle of attack of $180°$, the flow over the sharp airfoil edge produces a small separated flow region on the upper surface, after which the flow reattaches to the surface; the boundary layer is turbulent from the point of reattachment to the downstream separation point.

The impact of the trailing edge model is surprisingly small. The pressure coefficients for $170°$ and $180°$ shown in Fig. 6 indicate that primary differences are at the trailing edge, as expected. At $170°$ the O-grid exhibits an oscillation in pressure near the trailing edge that appears to be related to multi-frequency vortex shedding. The complexity of the flow over the upper surface is illustrated in the vorticity for the airfoil at $170°$ shown in Fig. 10.

Earlier computations with RANS turbulence models resulted in lift and moment changes with angle of attack that were $40 - 50\%$ lower than the data. Using Critzos' observations as a guide, the influence of laminar flow and transition was studied. It was observed that a boundary layer trip of $30\%c$ increased the lift curve slope near $180°$ so that it was much closer to the experimentally observed values. However, below $175°$, the lift and moment exhibited stall-like characteristics, indicating that the flow field character changes at that point. The integrated values also did not exhibit the stall drop experienced at about $169° - 171°$. When a three-dimensional, time-accurate advanced turbulence method was applied in this region, the behavior of the airfoil changed dramatically, reproducing the numerical results shown in this work.

Expanded views of Fig. 5 are shown in Fig. 11 for further analysis. The error bars indicate the highly unsteady nature of the flow in this region, due to the blunt trailing edge. Although the data do not match experiment exactly, the error bars indicate that the simulations are within the range of the numerically predicted physics, and some error due to digitization from the experimental data plots is to be expected. The lift curve slope is still about 10% below the experimental values, although the peak magnitude and location of the lift stall is reproduced, along with the post-stall behavior. The moment coefficient mimics this correlation of the lift coefficient. The numerical drag near $180°$ is about 10 counts lower than experiment, though this is within the digitization accuracy from the plots. The slope of the drag rise is comparable between the data.

Figure 10: Example of an instantaneous flow field simulated by a hybrid RANS-LES turbulence model for $\alpha = 170°$.

7.2. Yawed Flow

Rotor blades will encounter radial flow over some portion of the rotor disk in forward flight. There are correction models[29] for comprehensive and flight simulation codes that have been developed from classic yaw equivalence corrections that are made to blades in yawed flow. These corrections have been developed and tested for angles of attack and Mach number combinations that will typically be encountered in rotor advance ratios of 0.5 and less. It is uncertain how these models will behave at the more extensive angle of attack-Mach combinations that will be encountered in high-advance-ratio flight (Fig. 1). Therefore, a study was undertaken to further understand the character of the yawed flow with the aim of extracting additional understanding of the flow physics and behavior of these yaw correction models for high-advance-ratio flight conditions. Past experimental efforts were primarily limited to swept wings[23,28] at low ($typically < 20°$) angle of attack and Mach number combinations. These can be utilized to determine the validity of the numerical experiments.

7.2.1. Physics of yawed flow

The extraction of empirical formulas from a numerical experiment is dependent on the fidelity of the simulations used to obtain the underlying data from which equations are extracted. For the yawed flow simulations, a number of preliminary evaluations were accomplished to ensure high fidelity results. As discussed in a previous section, the influence of the spanwise grid extent and number of spanwise stations were first studied to provide assurance that the results include the three-dimensional components without contamination from the periodic boundary conditions. An $8c$ spanwise extent with 121 span stations was found to be necessary for the more rigorous (higher angle of attack and Mach number) flows where separation and shock interaction are important. The solutions in the nonlinear aerodynamic regime can take the form of a purely two-dimensional flow, as illustrated by the shock in Fig. 12(a), or a spanwise periodic flow shown in Fig. 12(b). In addition, the ability to correctly predict separation is key to correctly resolving these flows. While it is assumed that the flow is fully turbulent, there is a significant difference between the character of the flow and integrated quantities depending on the turbulence simulation method applied in the simulation.

Consider the NACA0012 infinite wing at $12°$ angle of attack and yaw of $40°$ at Mach 0.6 where Fig. 13 exemplifies the impact of the turbulence simulation technique. For the Menter kω-SST RANS turbulence model, isovorticity contours predict separation at about $0.01c$, with some vortex roll-up in the wake. The KES simulation of the same configuration shows very regular spanwise periodic vortex roll-up with separation between $0.10c - 0.11c$. Further analysis indicates that the RANS simulation is attempting to model the flow delineated by the KES results, but there is significant dissipation and smearing of the features in the unsteady flow field. The resulting difference in the integrated loads and moments is significant as the RANS results over predict the lift and drag coefficient values by 29% and 22%, respectively, compared to the KES simulation. The RANS solution also indicates a much larger negative pitching moment compared to the KES prediction. It should be noted that both of these runs were time-accurate simulations with the same grids, flight conditions, and timestep.

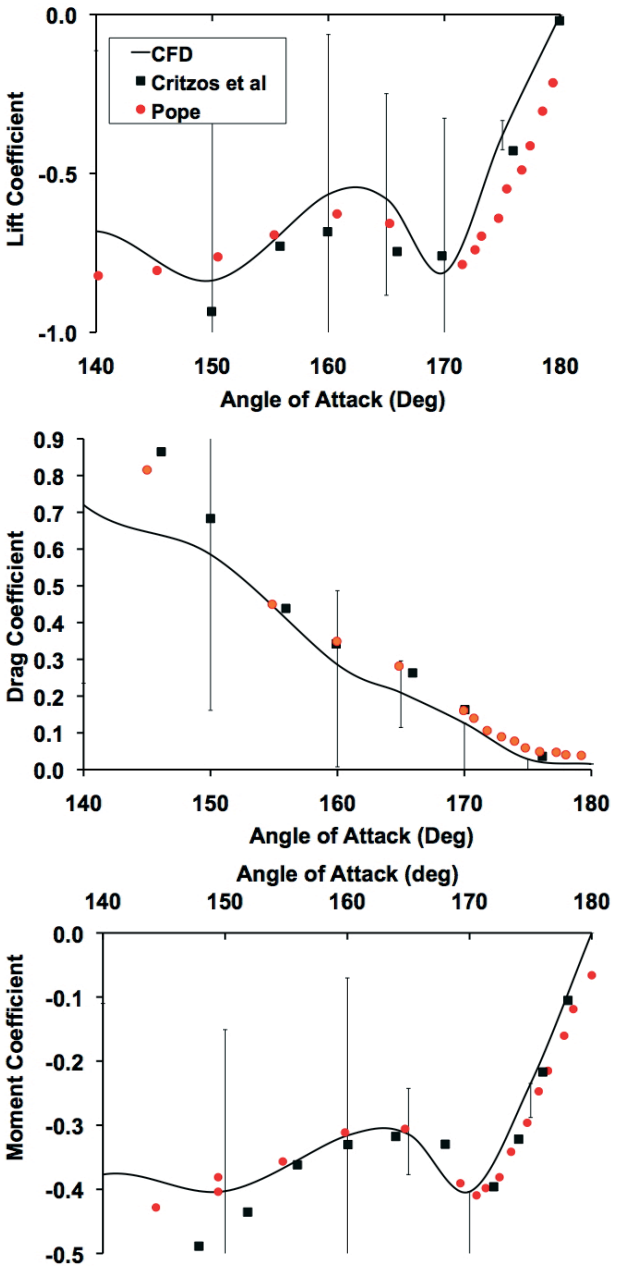

Figure 11: Mach 0.1 (incompressible) comparisons of kω-SST RANS simulations with Critzos[19] and Pope[18] experiments.

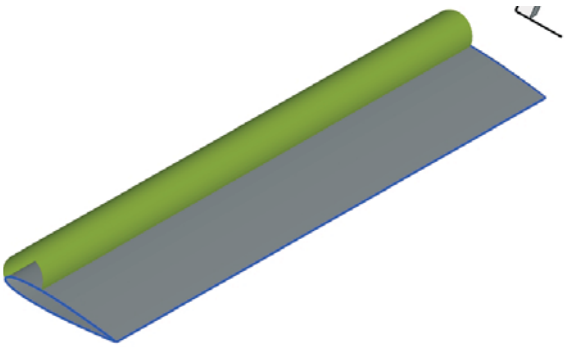

(a) Constant location shock zone

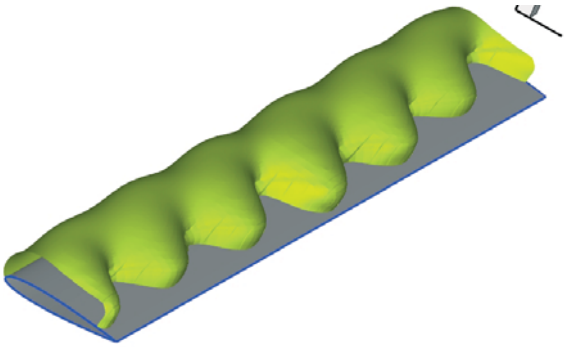

(b) Periodic vorticity during onset of stall

Figure 12: Verification of the infinite wing assumption for yawed flows.

7.2.2. Correlation with Experimental Data

In order to come to some conclusions from this study, the accuracy of the numerical simulations for the yawed flow needed to be evaluated. There are limited data from Purser and Spearman[24] that compare the lift curve slope within the linear aerodynamic range. While Purser and Spearman have data from multiple aspect ratios, their highest aspect ratio of 6 is the most appropriate to compare with the computational data. Fig. 16 compares these data with the numerical results, and it is seen that the correlation is within 10%, while the delta is between 0.02-0.03.

7.2.3. Evaluation of Empirical Yaw Corrections

The integrated force and moment data from the numerical experiments were correlated with the cross-flow correction model of Johnson,[29] which is based on the yaw equivalence principle. In this model, the lift, drag and moment coefficients on the normal blade section in yawed flow, c_ℓ,c_d,c_m, are obtained from the sectional (two-dimensional) coefficients for the unyawed flow, $c_{\ell_{2d}}$,$c_{d_{2d}}$,$c_{m_{2d}}$ by applying the following formulas:

$$
\begin{aligned}
c_\ell(\alpha) &= c_{\ell_{2d}}(\alpha cos^2\Lambda)/cos^2\Lambda \\
c_d(\alpha) &= c_{d_{2d}}(\alpha cos\Lambda)/cos\Lambda \\
c_m(\alpha) &= c_{m_{2d}}(\alpha cos^2\Lambda)/cos^2\Lambda
\end{aligned} \tag{6}
$$

The formulas are applied for a Mach number based on the velocity normal to the blade section, $M_n = V_n/a = M_\infty cos\Lambda$. The yawed flow also means that the airfoil behaves as a thinner airfoil ($t = t_y cos\Lambda$), however, this correction is not typically incorporated. The yawed section force and moment coefficients are related to the normal section coefficients in Eqn. 6 by the expressions $c_{\ell_y} = c_\ell cos^2\Lambda$, $c_{d_y} = c_d cos\Lambda$, and $c_{m_y} = c_m cos^2\Lambda$.

A sweep of Mach numbers ($M_\infty = 0.2 - 0.8$) and angle of attack ($\alpha = 0^\circ - 16^\circ$) combinations for yawed flow from $\Lambda = 0^\circ - 90^\circ$ was compared with the Johnson cross-flow model[29] to first verify that the computational data compares well at low angles of attack and Mach numbers where the model was designed to work well. Consider the case when the angle of attack is 4° over the subsonic Mach range, as illustrated by the yawed force and moment sectional coefficients (Fig. 14). This data set has a mix of subcritical and supercritical Mach numbers to examine the behavior of the model. It is found that the model works quite well over the full range of yaw angles for lift coefficient, while the drag model is less accurate. Not unsurprisingly, the poorest correlation is for the pitching moment, which is the most sensitive of the integrated quantities. As the angle of attack is increased, the correlation with the higher Mach angles is poorer, as exemplified in Fig. 15. The yawed lift correlations are well within 5% for subcritical Mach numbers, as are the yawed drag correlations. Average subcritical Mach number relative errors are about 5-8%. As the Mach number increases into the transonic regime, the errors increase significantly, in particular for the yawed moment coefficient, as observed in Fig. 15.

A second study was made for a high angle of attack sweep at the incompressible Mach range to examine the ability of the model to predict the characteristics of high angle of attack conditions that are well above the stall angle, even when yaw is applied. The results of this study are shown in Figs. 17 and 18. The model predicts the characteristics of yawed flow relatively well, except in areas where the yawed force and moment coefficients (Eqn. 6) are rapidly changing. This is readily observed, for example, when the equivalent yawed angle of attack values are near stall (Fig. 5).

The yaw equivalence models will asymptote to zero for lift and moment of the NACA0012 coefficients when the yaw angle approaches 90°, while drag goes to c_{d_o}. For

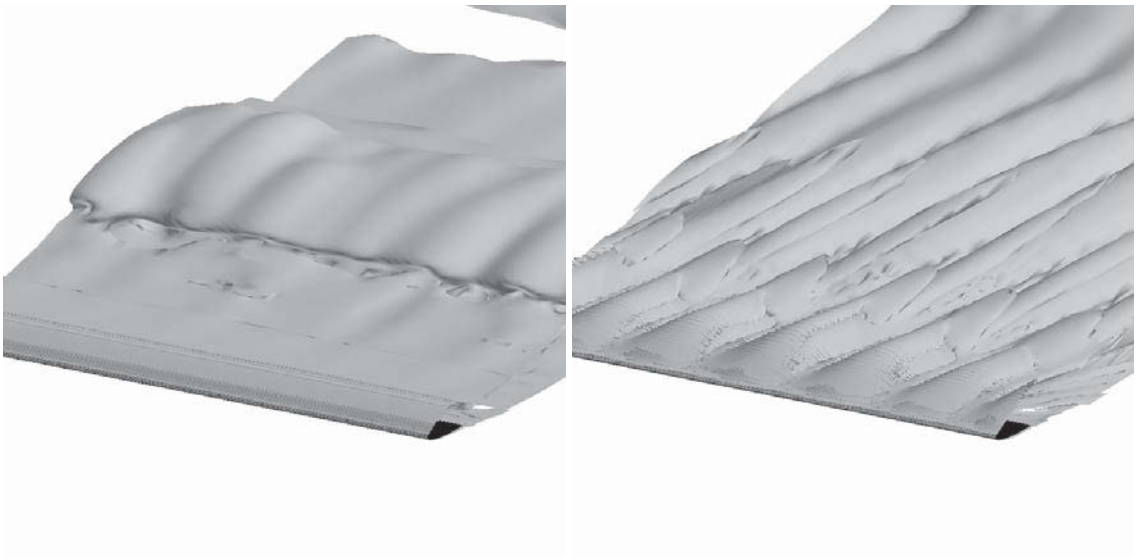

(a) Isovorticity contours

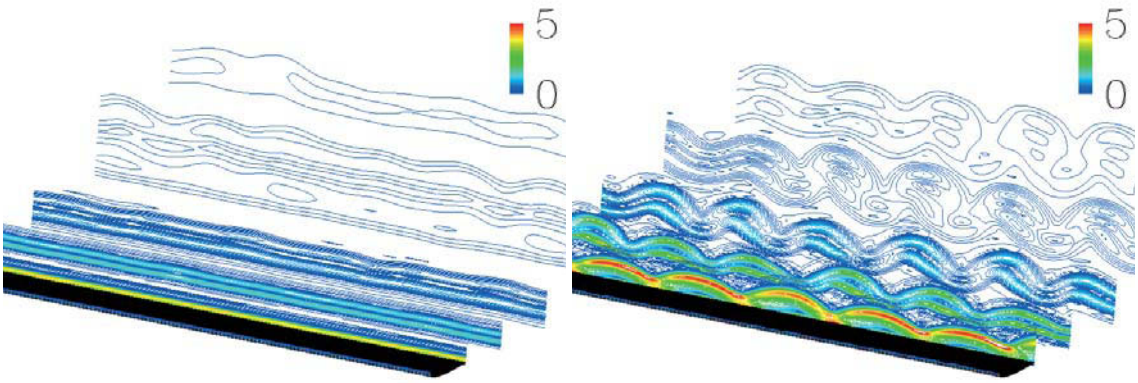

(b) Vorticity magnitude contour slices

Figure 13: Variation in yaw simulations due to turbulence modeling. Menter kω-SST RANS turbulence model is on the left, and KES LES-based turbulence simulation is on the right.

the Reynolds numbers studied here, Eqn. 2 derived[20] from experiment equates to a drag coefficient of 0.008–0.010 with an error of ± 0.005. These values are well predicted by the computational method, as discussed previously. Upon observing the cross-flow computational results at $\Lambda = 90°$, they are found to be between 3–4 counts of drag ($c_{d_{\Lambda=90°}} = 0.003 - 0.004$), no matter the free stream Mach number (subsonic) or angle of attack, as seen in Fig. 19. Further investigation shows that this drag result is approximately equal to the friction drag (c_f) of a flat plate at the Reynolds number of the simulation,[52] which corroborates the efficacy of the numerical method as it appears to correctly capture the change in the thickness. This result is only for the symmetric airfoil (NACA0012) used in this study, so that the impact of camber on the flat plate drag assumption is not yet known and should be investigated.

8. CONCLUSIONS

Extensive studies using numerical experiments were made for the NACA0012 airfoil over the full $0° - 180°$ range of angles of attack and yaw (sweep) angles from $0° - 90°$ and a smaller subset from $90° - 180°$. Correlation with known theory and experimental data where available were carried out. Several conclusions can be drawn from this work:

- Computational fluid dynamics methods will predict the lift, drag and moment within experimental limits for the linear aerodynamic regime given sufficient grid resolution. While the predictions are within experimental limits, L/D values continue to be under predicted, though advanced turbulence model predictions correlate better than RANS with experimental data.
- Three-dimensional simulations are necessary to capture the physics at and above stall, as the flow field may become quasi-periodic in the radial (span) direction. RANS methods will over or under predict the integrated loads and moments around the stall location as separation begins.
- The periodic boundary condition may force some aspect ratio effects (albeit much greater than the span to chord ratio of the computational grid) into the numerical simulations, even when the spanwise grid dependence is removed.
- Computational fluid dynamics simulations for yawed flows in the linear aerodynamic regime match typically within $3 - 5\%$ with the yaw equivalence theory.
- Using computational experiments, it is observed that the yaw equivalence correction breaks down in supercritical flow, in particular for pitching moment and drag, whose behavior are highly nonlinear in the transonic regime.
- The yaw equivalence correction works well at high angles of attack at lower Mach numbers, except when the corrected angles of attack fall near stall or where large excursions of the force and moment coefficients occur.
- For the NACA0012 in radial flow ($\Lambda = 90°$, the drag correlates well with flat plate drag at comparable Reynolds number, suggesting that a drag correction may be readily added to the yaw correction model.

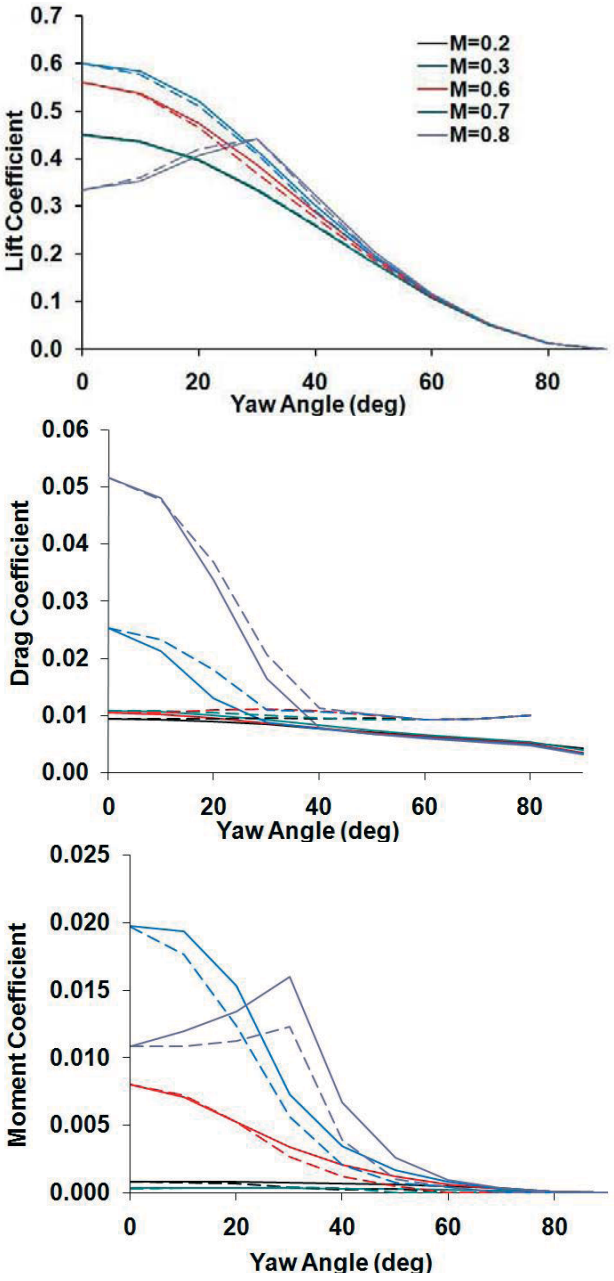

Figure 14: Yawed force and pitching moment characteristics of the NACA0012 infinite wing at $\alpha = 4°$. Solid lines are the CFD predictions while the dashed lines are predictions obtained by applying the model described in Eqn. 6 for cross-flow conditions.

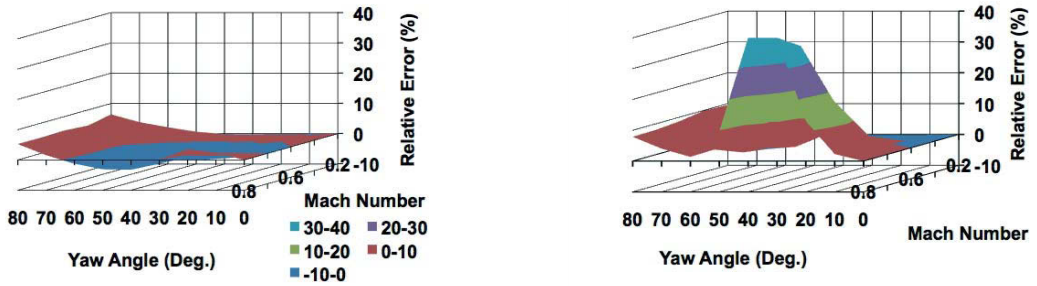

(a) Sectional lift coefficient

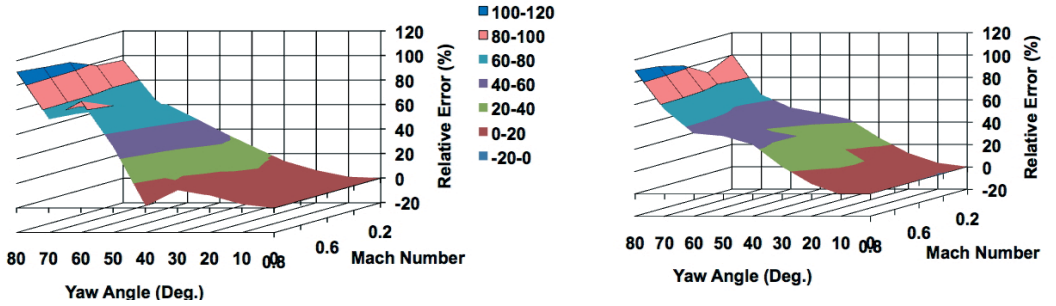

(b) Sectional drag coefficient

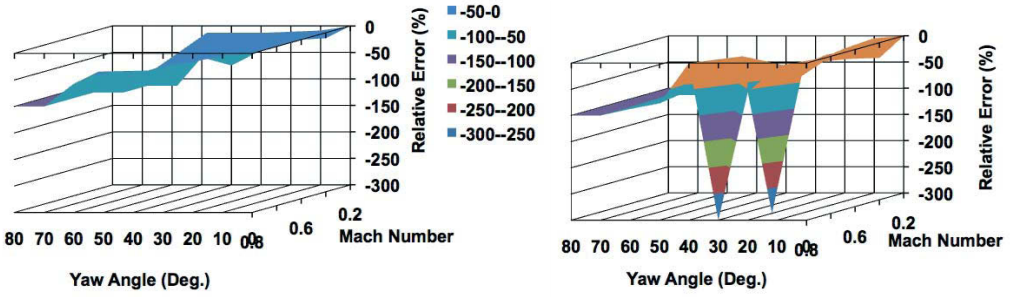

(c) Sectional pitching moment coefficient

Figure 15: Relative errors of the yaw equivalence theory to numerical predictions. Results for an angle of attack of 4° are on the left and 8° are on the right.

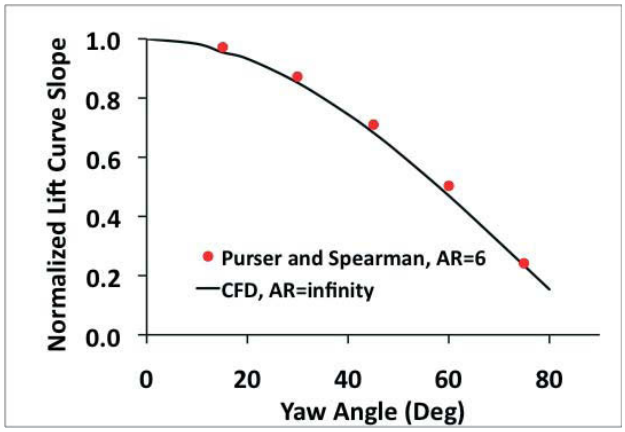

Figure 16: Correlation of the lift curve slope ratio ($c_\ell / c_{\ell_{\Lambda=0}}$) of CFD with Purser and Spearman experimental data.[24]

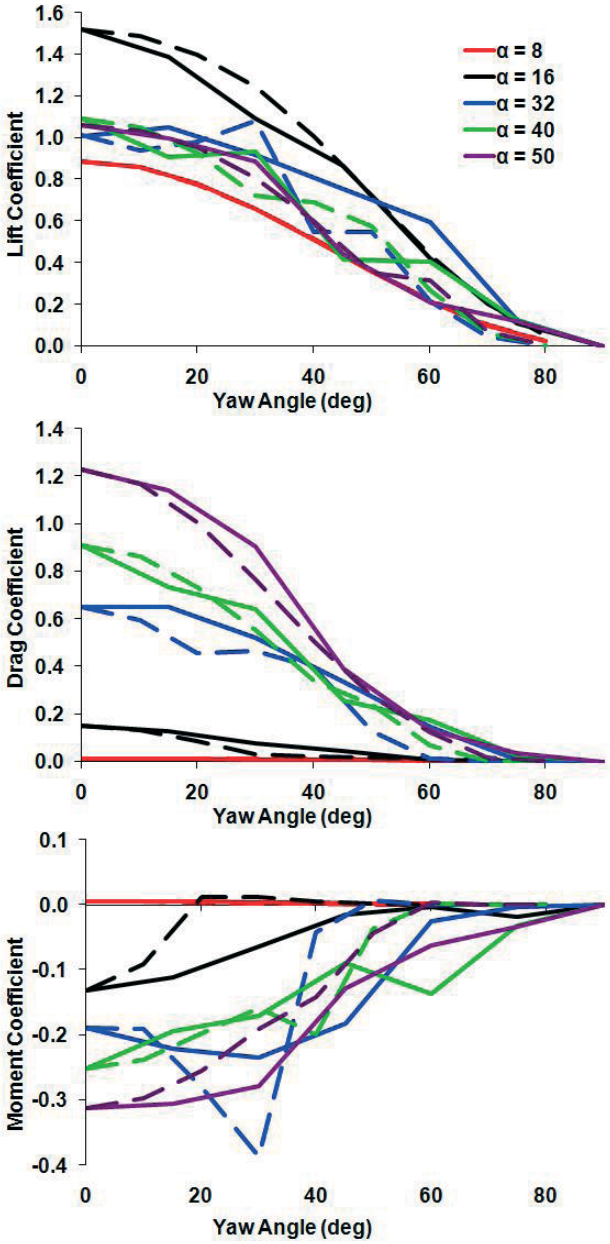

Figure 17: Comparison of the yaw equivalence model and CFD predictions in incompressible flow at angles of attack well above the stall angle. Solid lines are the CFD yawed flow computations, while dashed lines are the yawed model predictions.

9. ACKNOWLEDGMENTS

This work is supported via a NASA/Ames SBIR Phase II effort entitled “Next Generation Modeling Technology for High Speed Rotorcraft”. The technical monitor is Dr. William Warmbrodt. The authors would like to thank Dr. Warmbrodt and the NASA Advanced Supercomputing (NAS) Division at NASA Ames Research Center for the computational resources utilized as a part of this study. This study generated a large data set that required significant post-processing by a number of students at Georgia Tech, without whom this study could not have been completed. The authors would like to thank Ms. Ritu Marpu, as well as Messrs. Nicholas Liggett and Phillip Richards for their aid.

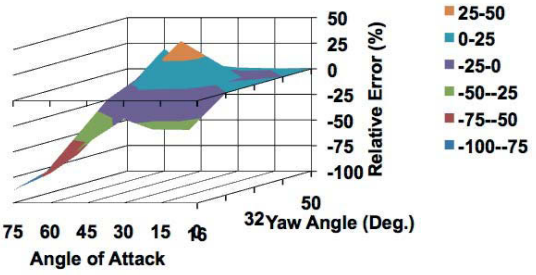

(a) Lift coefficient

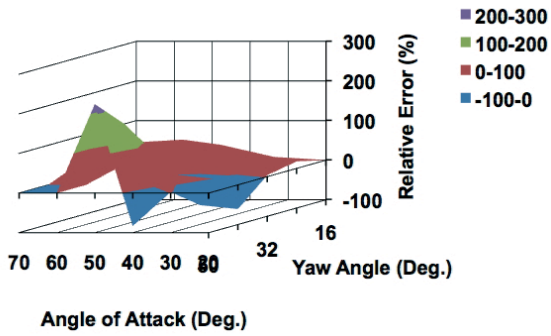

(b) Drag coefficient

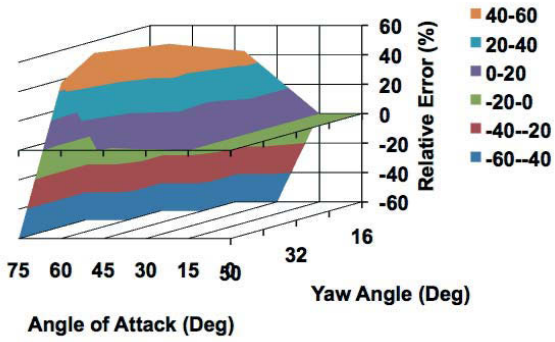

(c) Pitching moment coefficient coefficient

Figure 18: Relative errors of the yaw equivalence theory to numerical predictions in incompressible flow at angles of attack well above the stall angle.

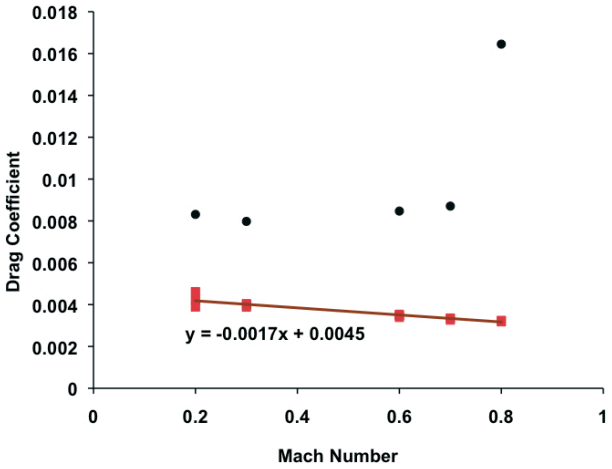

Figure 19: Comparison with the drag values at the limiting yaw angle ($c_{d_{\Lambda=90^\circ}}$) with the minimum drag of the airfoil.

References

[1] Kisielowski, E., Bumstead, R., Fissel, P., Chinsky, I., and DIV, B., "Generalized Rotor Performance." *U.S. Army Aviation Material Laboratories Technical Report 66-83, AD 648874*, 1966.

[2] Tanner, W., "Charts for Estimating Rotary Wing Performance in Hover and at High Forward Speeds," *NASA CR-114*, 1964.

[3] Sweet, G., Jenkins, J. L., and Winston, M. M., "Wind-Tunnel Measurements on a Lifting Rotor at High Thrust Coefficients and High Tip-Speed Ratios," *NASA TN D-2462*, 1964.

[4] Ekquist, D., "Design and Wind Tunnel Test of a Model Helicopter Rotor Having an Independently Moveable Inboard Blade Panel," , Boeing Co., Morton PA, Vertol Div, 1965.

[5] McCloud, J., Biggers, J., and Stroub, R., "An Investigation of Full-Scale Helicopter Rotors at High Advance Ratios and Advancing Tip Mach Numbers," *NASA TN D-4632*, 1968.

[6] McHugh, F. J. and Harris, F. D., "Have We Overlooked the Full Potential of the Conventional Rotor?" *Proceedings of the American Helicopter Society* 31^{st} *Annual Forum*, May 1975.

[7] Harris, F., Tarzanin Jr, F., and Fisher Jr, R., "Rotor high speed performance, theory vs. test," *Journal of the American Helicopter Society*, Vol. 15, No. 3, 1970, pp. 35–41.

[8] McCutcheon, R., "S-67 Flight Test Program," *Proceedings of the American Helicopter Society* 28^{th} *Annual Forum*, Vol. 28, 1972.

[9] Albers, J. and Zuk, J., "Civil Applications of High Speed Rotorcraft and Powered Lift Aircraft Configurations," *International Powered Lift Conference and Exposition, Santa Clara, CA, Proceedings*, Vol. 7, May 1987.

[10] Foster, M., "Commercial Quad Tiltrotor," *Proceedings of the American Helicopter Society* 58^{th} *Annual Forum*, June 2002.

[11] Williams, R., Rosenstein, H., and Wilkerson, J., "Advanced Technology Vertical Lift Airliner," *Proceedings of the American Helicopter Society* 58^{th} *Annual Forum*, American Helicopter Society, Inc, June 2002, pp. 188–229.

[12] Karem, A., "Optimum speed tilt rotor," Nov. 4 2003, US Patent 6,641,365.

[13] Carter, J., "Extreme mu rotor," 2006, US Patent 6,986,642.

[14] Johnson, W., Yamauchi, G., and Watts, M., "NASA Heavy Lift Rotorcraft Systems Investigation," NASA TP 213467, 2005.

[15] Ashby, D. and Eadie, W., "High Speed Rotorcraft Concepts," *Proceedings of the American Helicopter Society* 58^{th} *Annual Forum*, Vol. 58, American Helicopter Society, Inc, 2002, pp. 254–267.

[16] Quackenbush, T. R. and Wachspress, D. A., "Measurement and Analysis of High Advance Ratio Rotor Performance," *Proceedings of the American Helicopter Society Annual Forum*, Vol. 64, American Helicopter Society, Inc, April-May 2008.

[17] Sissingh, G., "Dynamics of rotors operating at high advance ratios," *Journal of the American Helicopter Society*, Vol. 13, No. 3, 1968, pp. 56–63.

[18] Pope, A., "The Forces and Pressures over an NACA 0015 Airfoil through 180 Degrees Angle of Attack," , Georgia Institute of Technology, 1947.

[19] Critzos, C., Heyson, H., and Boswinkle Jr, R., "Aerodynamic characteristics of NACA 0012 airfoil section at angles of attack from 0 to 180," NACA TN-3361, 1955.

[20] McCroskey, W., "A Critical Assessment of Wind Tunnel Results for the NACA 0012 Airfoil," NASA TM-100010, 1987.

[21] Bousman, W., "Aerodynamic Characteristics of SC1095 and SC1094 R8 Airfoils," TP-212265, NASA Ames Research Center, 2003.

[22] Smith, M., Wong, T., Potsdam, M., Baeder, J., and Phanse, S., "Evaluation of CFD to Determine Two-Dimensional Airfoil Characteristics for Rotorcraft Applications," *American Helicopter Society 60 th Annual Forum, Baltimore, MD*, 2004.

[23] Purser, P. E. and Spearman, M. L., "Wind-Tunnel Tests at Low Speed of Swept and Yawed Wings Having Various Plan Forms," NACA RML7D23, May 1947.

[24] Purser, P. E. and Spearman, M. L., "Wind-Tunnel Tests at Low Speed of Swept and Yawed Wings Having Various Plan Forms," NACA TN 2445, December 1951.

[25] St Hilaire, A., Carta, F., Fink, M., and Jepson, W., "The Influence of Sweep on the Aerodynamic Loading of an Oscillating NACA 0012 Aerofoil," NASA CR-3092, 1979.

[26] St. Hilaire, A. and Carta, F., "Analysis of Unswept and Swept Wing Chordwise Pressure Data from an Oscillating NACA 0012 Airfoil Experiment," NASA CR-3567, 1983.

[27] Lorber, P. F., Covino, A. F. J., and Carta, F. O., "Dynamic Stall Experiments on a Swept Three-Dimensional Wing in Compressible Flow," *Proceedings of the 22nd Fluid Dynamics, Plasma Dynamics & Lasers Conference*, AIAA, June 1991.

[28] Lorber, P. F., "Dynamic Stall of Sinusoidally Oscillating Three-Dimensional Swept and Unswept Wings in Compressible Flow," *Annual Forum Proceedings - American Helicopter Society*, 1992, pp. 1307–1322.

[29] Johnson, W., *Helicopter theory*, Dover publications, 1994.

[30] Harris, F., 2006, private communication.

[31] Strawn, R., Caradonna, F., and Duque, E., "30 Years of Rotorcraft Computational Fluid Dynamics Research and Development," *Journal of the American Helicopter Society*, Vol. 51, No. 1, 2006.

[32] Wilcox, D., *Turbulence modeling for CFD*, La Canada, CA: DCW Industries, Inc, 1993.

[33] Shelton, A., Abras, J., Hathaway, B., Sanchez-Rocha, M., Smith, M., and Menon, S., "An Investigation of the Numerical Prediction of Static and Dynamic Stall," *Proceedings of the American Helicopter Society* 61^{st} *Annual Forum*, American Helicopter Society, Inc, 2005.

[34] Jespersen, D., Pulliam, T., and Buning, P., "Recent enhancements to OVERFLOW," No. AIAA-97-0644, 1997.

[35] Chan, W., Meakin, R., and Potsdam, M., "CHSSI software for geometrically complex unsteady aerodynamic applications," No. AIAA-01-0593, 2001.

[36] Buning, P., Gomez, R., and Scallion, W., "CFD approaches for simulation of wing-body stage separation," No. AIAA-04-4838, 2004.

[37] Steger, J., Dougherty, F., and Benek, J., "A Chimera grid scheme," *American Society of Mechanical Engineers, New York*, 1993, pp. 59–69.

[38] Roe, P., "Approximate Riemann solvers, parameter vectors, and difference schemes," *Journal of computational physics*, Vol. 135, No. 2, 1997, pp. 250–258.

[39] Spalart, P. and Allmaras, S., "A one-equation turbulence model for aerodynamic flows," *AIAA, Aerospace Sciences Meeting and Exhibit, 30 th, Reno, NV*, 1992, p. 1992.

[40] Menter, F., "Two-equation eddy-viscosity turbulence models for engineering applications," *AIAA journal*, Vol. 32, No. 8, 1994, pp. 1598–1605.

[41] Fang, Y. and Menon, S., "A Two-Equation Subgrid Model for Large-Eddy Simulation of High Reynolds Number Flows," AIAA-06-0116, Reno, NV, Jan. 2006.

[42] Fang, Y. and Menon, S., "Kinetic Eddy Simualtion of Static and Dynamic Stall," *25th AIAA Applied Aerodynamics Conference, San Francisco, CA*, 2006.

[43] Sanchez-Rocha, M., Kirtas, M., and Menon, S., "Zonal Hybrid RANS-LES Method for Static and Oscillating Airfoils and Wings," 44^{th} *AIAA Aerospace Sciences Meeting*, January 2006.

[44] Sanchez-Rocha, M., *Wall-models for large eddy simulation based on a generic additive-filter formulation*, Ph.D. thesis, Georgia Institute of Technology, december 2008.

[45] Spalart, P., Jou, W., Strelets, M., and Allmaras, S., "Comments on the feasibility of LES for wings, and on a hybrid RANS/LES approach," *Advances in DNS/LES*, Vol. 1, 1997.

[46] Lynch, C. and Smith, M., "Hybrid RANS-LES turbulence models on unstructured grids," No. AIAA–08–3854, 2008.

[47] Shelton, A. B., Braman, K., Smith, M. J., and Menon, S., "Improved Turbulence Modeling for Rotorcraft," *(to appear)Journal of the American Helicopter Society*, 2010.

[48] Abbott, I. H. and von Doenhoff, A. E., *Theory of Wing Sections*, Dover publications, 1959.

[49] Jacobs, E. N. and Sherman, A., "Airfoil Section Characteristics as Affected by Variations of the Reynolds Number," TR-586, NASA Langley Research Center, 1939.

[50] Hoerner, S., *Fluid-dynamic drag*, Hoerner fluid dynamics Brick Town, NJ, 1965.

[51] Wieselsberger, C., "Airplane Body (Non Lifting System) Drag and Influence on Lifting System." *Aerodynamic Theory (Vol. IV)*, Julius Springer (Berlin), 1935, pp. 141–146.

[52] Schlichting, H., Gersten, K., Krause, E., Mayes, K., and Oertel, H., *Boundary-layer theory*, Springer Verlag, 2000.